Transportation Research Part C 95 (2018) 445–459

Contents lists available at ScienceDirect

Transportation Research Part C

journal homepage: www.elsevier.com/locate/trc

Connected cruise control among human-driven vehicles: Experiment-based parameter estimation and optimal control design

Jin I. Ge[a,b,*], Gábor Orosz[a]

[a] Department of Mechanical Engineering, University of Michigan, Ann Arbor, MI 48109, USA
[b] Department of Computing and Mathematical Sciences, California Institute of Technology, Pasadena, CA 91125, USA

ARTICLE INFO

Keywords:
Connected automated vehicle
Human driving behavior
Sweeping least square method
Optimal control

ABSTRACT

In this paper, we consider connected cruise control design in mixed traffic flow where most vehicles are human-driven. We first propose a sweeping least square method to estimate in real time feedback gains and driver reaction time of human-driven vehicles around the connected automated vehicle. Then we propose an optimal connected cruise controller based on the mean dynamics of human driving behavior. We test the performance of both the estimation algorithm and the connected cruise control algorithm using experimental data. We demonstrate that by combining the proposed estimation algorithm and the optimal controller, the connected automated vehicle has significantly improved performance compared to a human-driven vehicle.

1. Introduction

Over the past few decades, passenger vehicles are equipped with more and more automation features during the efforts to improve active safety, passenger comfort, and traffic efficiency of the road transportation system. In particular, adaptive cruise control (ACC) was invented to alleviate human drivers from the constant burden of speed control (Labuhn and Chundrlik, 1995). While the influence of ACC is yet to be observed in real traffic due to its low penetration rate, theoretical studies have found that ACC-equipped vehicles may only have limited benefits on traffic flow (Vander Werf et al., 2002; van Arem et al., 2006; Shladover et al., 2012). In particular, ACC vehicles may not be able to effectively suppress the speed fluctuations propagating through the vehicle string, as each ACC vehicle only responds to its immediate predecessor (Barber et al., 2009).

In order to overcome such limitations in an ACC-equipped vehicle platoon, cooperative adaptive cruise control (CACC) has been proposed using vehicle-to-vehicle (V2V) and vehicle-to-infrastructure (V2I) communication (Milanes et al., 2011; Wang et al., 2014; Ploeg et al., 2014b; Ploeg et al., 2014a; Milanes and Shladover, 2014; di Bernardo et al., 2015; Wang, 2018). CACC has been shown to improve fuel economy and traffic efficiency both in theory and in experiments (Li et al., 2015; Zhou et al., 2017; Lioris et al., 2017; Li et al., 2017a; Li et al., 2017b; Li et al., 2017c). However, the application of CACC in the early stages of driving automation may be significantly limited by the requirement that all vehicles in a CACC platoon be equipped with ACC aside from V2X communication devices (van Nunen et al., 2012; Englund et al., 2016). In particular, (Shladover et al., 2015) commented that “at low market penetrations, ··· the probability of consecutive vehicles being equipped is negligible”. Since V2X devices have relatively low cost compared with ACC and other driving automation systems, it is desirable to exploit the benefits of V2X without being restricted by the penetration rate of ACC. Thus, we need to consider a connected automated vehicle design that is able to utilize V2X information in partially connected and automated environment (Jiang et al., 2017; Zhao et al., 2018; Fountoulakis et al., 2017).

* Corresponding author at: Department of Computing and Mathematical Sciences, California Institute of Technology, Pasadena, CA 91125, USA.
E-mail addresses: gejin@umich.edu (J.I. Ge), orosz@umich.edu (G. Orosz).

https://doi.org/10.1016/j.trc.2018.07.021
Received 10 August 2017; Received in revised form 23 July 2018; Accepted 23 July 2018

For the longitudinal control of such a connected automated vehicle, we proposed a class of connected cruise controllers (CCC) that exploit ad hoc V2V communication with multiple human-driven vehicles ahead (Orosz, 2016; Ge et al., 2018). Indeed, connected cruise control can be viewed as an "advanced CACC implementation that adds information from vehicles that are beyond the direct line of sight" (Shladover et al., 2015). By utilizing motion information from multiple vehicles ahead, connected cruise control is able to gain "phase lead" as it responds to speed fluctuations propagating through the vehicles (Orosz et al., 2017). Several theoretical studies have shown that connected cruise control is able to significantly improve active safety, fuel economy, and traffic efficiency of the connected automated vehicle, especially by providing head-to-tail string stability (Zhang and Orosz, 2016; Ge and Orosz, 2014; Avedisov and Orosz, 2017; Orosz, 2016; Ge et al., 2016).

However, previous studies generally assumed that the connected automated vehicle has a priori knowledge on the dynamics of its predecessors (Zhang and Orosz, 2016; Ge and Orosz, 2014; Qin and Orosz, 2017). While such an assumption may hold for a platoon of pre-assigned automated vehicles (Ploeg et al., 2014b; van Nunen et al., 2012; Englund et al., 2016), it will not hold for a system where a connected automated vehicle drives behind several human-driven vehicles. Therefore, to create "comprehensive preview" about incoming traffic perturbations based on motion information farther ahead (Shladover et al., 2015), the driving parameters of preceding human-driven vehicles need to be estimated. Once the human car-following behavior can be described quantitatively, connected automated vehicle designs can be implemented among human-driven vehicles in real traffic, and the benefits of V2V can be harvested beyond platoons of automated vehicles.

While the steady-state driving behavior of individual cars can be deduced from aggregated traffic data, driving parameters such as the feedback gains and driver reaction time delay need to be estimated based on the trajectories of individual cars. While feedback gains can be estimated in delay-free systems using Lyapunov-type methods (Diop et al., 2001; Gomez et al., 2007) and data-driven methods (Monteil and Bouroche, 2016; Lin et al., 2018), it is still challenging to estimate the delay time and feedback gains simultaneously (Orlov et al., 2003; Drakunov et al., 2006; Ge and Orosz, 2016). Moreover, stringent convergence conditions often make Lyapunov-type methods unrealistic for human parameter estimation in real-world traffic. Thus, in this paper we propose a sweeping least square method to simultaneously estimate human feedback gains and reaction time delay using motion information received through V2V, in particular the dedicated short range communication (DSRC). By testing the sweeping least squares algorithm with experimental data, we obtain the distributions and variations of human feedback gains and driver reaction time. Then, using the optimal connected cruise control framework established in Ge and Orosz (2017), we design a connected cruise controller and demonstrate the performance improvements of the connected automated vehicle following human-driven vehicles. While stochastic perturbations and gains in human-driven vehicles have been considered (Moser et al., 2018; Chen et al., 2018), this CCC design is among the first efforts to consider stochastic reaction time delay in human-driven vehicles.

The rest of this paper is organized as follows: in Section 2 we describe a theoretical car-following model for human-driven vehicles; in Section 3 we propose a sweeping least square method to estimate driving parameters for human drivers; in Section 4 we validate the estimation algorithm in a four-car experiment and discuss the variation and distribution of human parameters; in Section 5 we design an optimal connected cruise controller based on the average human car-following behavior and demonstrate the performance improvement; and finally in Section 6 we conclude the results and discuss future research directions.

2. Theoretical car-following model

In this section, we consider the longitudinal motion of vehicles in a single lane; see Fig. 1(a), and introduce the theoretical car-following model in non-emergency situations (Helbing, 2001; Treiber et al., 2006; Orosz et al., 2010). The dynamics of a conventional vehicle i is

$$\begin{aligned} \dot{h}_i(t) &= v_{i+1}(t)-v_i(t), \\ \dot{v}_i(t) &= \alpha_i(V_i(h_i(t-\tau_i))-v_i(t-\tau_i)) + \beta_i(v_{i+1}(t-\tau_i)-v_i(t-\tau_i)). \end{aligned} \tag{1}$$

Here the dot stands for differentiation with respect to time t, h_i denotes the spacing, (i.e., the bumper-to-bumper distance between the vehicle i and its predecessor), and v_i denotes the velocity of vehicle i; see Fig. 1(a). According to (1) the acceleration is determined

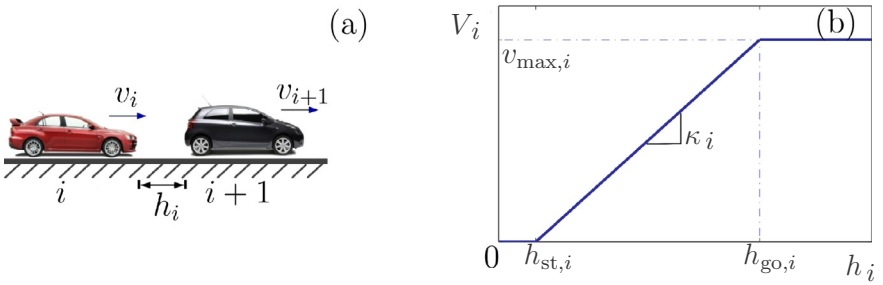

Fig. 1. (a): Single-lane car-following of human-driven vehicles showing the spacing and the velocities. (b): The range policy (2) where $v_{\max,i}$ is the maximum velocity, $h_{\mathrm{st},i}$ is the smallest spacing before the vehicle intends to stop, and $h_{\mathrm{go},i}$ is the largest spacing after which the vehicle intends to maintain $v_{\max,i}$.

by two terms: the difference between the spacing-dependent desired velocity and the actual velocity, and the velocity difference between the vehicle and its predecessor. The gains α_i and β_i are used to correct velocity errors, and τ_i is the driver reaction time.

The desired velocity is determined by the range policy function

$$V_i(h_i) = \begin{cases} 0 & \text{if} \quad h_i \leqslant h_{\mathrm{st},i}, \\ \kappa_i(h_i - h_{\mathrm{st},i}) & \text{if} \quad h_{\mathrm{st},i} < h_i < h_{\mathrm{go},i}, \\ v_{\mathrm{max},i} & \text{if} \quad h_i \geqslant h_{\mathrm{go},i}, \end{cases} \tag{2}$$

shown in Fig. 1(b). That is, the desired velocity is zero for small spacings ($h_i \leqslant h_{\mathrm{st},i}$) and equal to the maximum speed $v_{\mathrm{max},i}$ for large spacings ($h_i \geqslant h_{\mathrm{go},i}$). Between these, the desired velocity increases with the spacing linearly, with gradient κ_i. Many other range policies may be chosen, but the qualitative dynamics remain similar if the above characteristics are kept (Orosz et al., 2010).

We note that (1), (2) bears resemblance to many ACC designs (Labuhn and Chundrlik, 1995; Barber et al., 2009). In particular, when $h_{\mathrm{st},i} < h_i < h_{\mathrm{go},i}$, both the ACC designs and the theoretical car-following model (1), (2) contain feedback terms with respect to the spacing distance h_i, the vehicle speed v_i, and the preceding vehicle's speed v_{i+1}. Also, the inverse of the range policy gradient κ_i is often referred to as the time gap in the ACC designs.

We also note that (2) defines the steady-state behavior of vehicle i, and in aggregation the steady-state traffic flow where vehicles travel with the same constant velocity:

$$h_i(t) \equiv h_i^*, \quad v_i(t) \equiv v^* = V_i(h_i^*). \tag{3}$$

In a vehicle string, the equilibrium velocity v^* is determined by the head vehicle while the equilibrium spacing h_i^* can be calculated from the range policy (2).

While (h^*, v^*) can be deduced from aggregated traffic data, there has been few research in the past investigating the distribution and variation of parameters α_i, β_i, κ_i, τ_i for individual vehicles, especially when they are human-driven. However, as geolocation, inertial measurement units and wireless communication devices become less expensive and more widespread, the time is ripe for such investigations. In particular, the knowledge of human driving behavior may be used to optimize the performance of a connected automated vehicle among human-driven cars. In this way, the benefits of V2V communication can be exploited without the support of other automated vehicles.

3. The sweeping least squares method

In this section we present a sweeping least squares method to simultaneously identify the feedback gains α_i, β_i, range policy slope κ_i, and delay time τ_i in (1) for human-driven vehicles. We assume that the spacing and velocity data of human-driven vehicles can be obtained through V2V communication. The estimation will be used in the next section to design connected cruise controllers that exploit motion information of these human-driven vehicles.

Note that when $h_{\mathrm{st},i} < h_i < h_{\mathrm{go},i}$ a human driver maintains affine spacing and speed feedback terms, and all parameters α_i, β_i, κ_i, τ_i can be estimated, cf. (1), (2). When the spacing is too large ($h_i > h_{\mathrm{go},i}$) or too small ($h_i < h_{\mathrm{st},i}$), the range policy function (2) saturates and information on the gradient κ_i is lost. Since the value of κ_i significantly influences the string stability (Seiler et al., 2004; Zhang and Orosz, 2016), we focus on the region $h_{\mathrm{st},i} < h_i < h_{\mathrm{go},i}$, where uniform traffic flow may turn into stop-and-go traffic jams (Orosz et al., 2010). Therefore, we consider the motion of the human-driven vehicle i for $h_{\mathrm{st},i} < h_i < h_{\mathrm{go},i}$

$$\begin{aligned} \dot{\widehat{h}}_i(t) &= v_{i+1}(t) - v_i(t), \\ \dot{v}_i(t) &= \alpha_i(\kappa_i \widehat{h}_i(t-\tau_i) - v_i(t-\tau_i)) + \beta_i(v_{i+1}(t-\tau_i) - v_i(t-\tau_i)), \end{aligned} \tag{4}$$

where $\widehat{h}_i = h_i - h_{\mathrm{st},i}$.

We discretize the second equation in (4) using the explicit Euler method with time step Δt:

$$\frac{v_i[k+1] - v_i[k]}{\Delta t} = \alpha_i(\kappa_i \widehat{h}_i[k-m] - v_i[k-m]) + \beta_i(v_{i+1}[k-m] - v_i[k-m]). \tag{5}$$

where $m = \mathrm{round}(\tau_i/\Delta t)$. Here $\Delta t = 0.1$ [s] as the update frequency of V2V communication is 10 Hz.

We consider $N+1$ data points over a timespan of $N\Delta t$ and rewrite the unknown parameters α_i, β_i, κ_i in (5) as

$$a = -\alpha_i - \beta_i, \quad b = \alpha_i \kappa_i, \quad c = \beta_i. \tag{6}$$

We consider the possible range of driver reaction time $\tau_i \in [\tau_{\min}, \tau_{\max}]$, and sample it such that $\tau_i = m\Delta t$, where $m \in \{m_{\min}, \ldots, m_{\max}\}$ with $\tau_{\min} = m_{\min}\Delta t$ and $\tau_{\max} = m_{\max}\Delta t$. Then for each potential unit of delay m, the corresponding gains are

$$\begin{bmatrix} \widetilde{a}(m) \\ \widetilde{b}(m) \\ \widetilde{c}(m) \end{bmatrix} = (\mathbf{A}^{\mathrm{T}}\mathbf{A})^{-1}\mathbf{A}^{\mathrm{T}}\mathbf{B}(m), \tag{7}$$

and the corresponding minimum fitting error under delay $m\Delta t$ is

$$R^*(m) = \min_{a,b,c} R(a,\, b,\, c;m) = \left\| \mathbf{A} \begin{bmatrix} \widetilde{a}\,(m) \\ \widetilde{b}\,(m) \\ \widetilde{c}\,(m) \end{bmatrix} - \mathbf{B}(m) \right\|^2, \tag{8}$$

where

$$\mathbf{A} = \begin{bmatrix} v_i[0] & \widehat{h}_i[0] & v_{i+1}[0] \\ \vdots & \vdots & \vdots \\ v_i[N] & \widehat{h}_i[N] & v_{i+1}[N] \end{bmatrix}, \quad \mathbf{B}(m) = \frac{1}{\Delta t} \begin{bmatrix} v_i[m+1] - v_i[m] \\ \vdots \\ v_i[m+N+1] - v_i[m+N] \end{bmatrix}, \tag{9}$$

with the data size N larger than the maximum delay unit $m_{\max}$.

Among the potential delay values, we choose the delay $\widetilde{\tau}_i = \widetilde{m}\Delta t$ and its corresponding estimated gains $\widetilde{\alpha}$, $\widetilde{\beta}$, $\widetilde{\kappa}$ which generate the smallest fitting error. That is,

$$\widetilde{m} = \arg\min_m R^*(m), \quad \widetilde{\alpha}_i = -\widetilde{a}\,(\widetilde{m}) - \widetilde{c}\,(\widetilde{m}), \quad \widetilde{\beta}_i = \widetilde{c}\,(\widetilde{m}), \quad \widetilde{\kappa}_i = \widetilde{b}\,(\widetilde{m})/\widetilde{\alpha}_i. \tag{10}$$

We note that each least square calculation (7), (9) exhibits a small computational load. Thus, the estimation algorithm (7), (9), (8), (10) can be implemented in real time.

4. Experimental validation of estimation algorithm

In this section we test the sweeping least squares method using experimental data and discuss the variation and distribution of estimated human parameters.

We equip four production vehicles with on-board units that receive and broadcast V2V messages through DSRC; see Fig. 2. The on-board units also record GPS coordinates (latitude ϕ, longitude λ, elevation r) and speed v of each vehicle in every 0.1 [s]. The experiments are conducted on a local single-lane road where the four vehicles are driven in a string by human drivers; see Fig. 3(a). Then the spacing for vehicle i is

$$h_i = d_{i(i+1)} - l, \tag{11}$$

where $l = 5$ [m] is the assumed vehicle length, and $d_{i(i+1)}$ is the great-circle distance between two GPS points (ϕ_i, λ_i, r_i) and $(\phi_{i+1}, \lambda_{i+1}, r_{i+1})$, which is given by the Haversine formula

$$d_{i(i+1)} = 2\left(R + \frac{r_i + r_{i+1}}{2}\right) \arcsin \sqrt{\sin^2\left(\frac{\phi_i - \phi_{i+1}}{2}\right) + \cos\phi_i \cos\phi_{i+1} \sin^2\left(\frac{\lambda_i - \lambda_{i+1}}{2}\right)}, \tag{12}$$

cf. (Inman, 1835). In this paper, we set the nominal radius of the Earth $R = 6371000$ [m]. The spacing and velocity profiles from one of the test runs are shown in Fig. 3(b,c).

In Fig. 3(c) we can see that the velocity v_4 of the head vehicle (green curve) is almost constant before decreasing at $t \approx 30$ [s], while the velocities of following vehicles oscillate before 30 [s] and they also exhibit more severe decelerations (v_3 is the black curve, v_2 is the red curve, v_1 is the blue curve). This shows that human drivers amplify the velocity fluctuations propagating along the chain. Such amplifications are often referred to as string instability (Seiler et al., 2004), which not only negatively impacts the performance of individual cars, but may also lead to stop-and-go traffic jams and rear-end crashes in heavy traffic. However, the motion information of vehicles 2,3,4 can be used by vehicle 1 to better reject the speed fluctuations (Shladover et al., 2012), if their car-following behaviors can be described quantitatively. Therefore, we apply the proposed estimation algorithm to the experimental data to observe the variation in the estimated driver parameters and their distributions.

The estimation algorithm (7), (9), (8), (10) produces $\widetilde{\alpha}_i$, $\widetilde{\beta}_i$, $\widetilde{\kappa}_i$, $\widetilde{\tau}_i$ for each data segment of size $N + 1$. For example, at time stamp $t_0 = k_0\Delta t$ an estimation is obtained using the motion information $v_i[k]$, $h_i[k]$, and $v_{i+1}[k]$ for $k \in \{k_0 - N, \ldots, k_0\}$. As the car receives

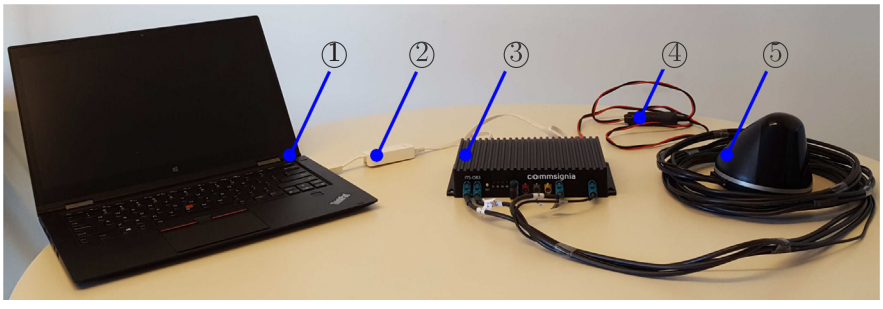

Fig. 2. The V2V communication on-board unit: ① upper-level computer, ② ethernet cable, ③ electronic control unit, ④ power cable, ⑤ V2V/GPS antennae.

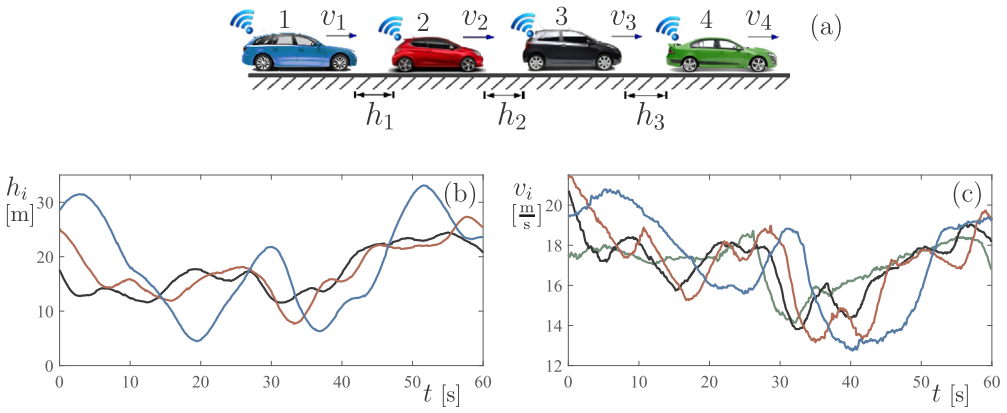

Fig. 3. (a) The experimental setup: a string of 4 vehicles on a single-lane road where all vehicles are equipped with GPS and V2V devices. (b,c) Headway and velocity profiles of the 4-vehicle string during one test run, where the black, red, and light blue curves correspond to the spacing and velocity profiles of vehicles 3, 2, 1, respectively. The green curve in (b) is the velocity of the head vehicle 4. (For interpretation of the references to color in this figure legend, the reader is referred to the web version of this article.)

new motion information and the window shifts forward in time, the estimated values of $\widetilde{\alpha}_i$, $\widetilde{\beta}_i$, $\widetilde{\kappa}_i$, and $\widetilde{\tau}_i$ change. Thus, the estimated parameters will be time-varying.

As an example, we estimate the driver parameters α_2, β_2, κ_2, τ_2 for vehicle 2 using h_2, v_2, v_3. The spacing h_2 is shown in Fig. 4(a), and the velocities v_2 (red curve) and v_3 (black curve) are shown in Fig. 4(b). We consider the minimum human reaction time $\tau_{\min} = 0.2$ [s] and maximum human reaction time $\tau_{\max} = 2$ [s], that is, the discrete time delay $m \in \{2, \ldots, 20\}$. Based on the observed spacing and velocity data, we also consider $h_{\mathrm{st},i} = 0$ [m], although $h_{\mathrm{st},i}$ may be non-zero in other driving scenarios. Finally, we consider $N = 150$ in each data segment, and correspondingly the parameter estimation starts at $t = 15$ [s], as shown in Fig. 5. As the data window moves forward in time, the estimated delay time $\widetilde{\tau}_2$ varies around 1 [s]; see Fig. 5(a). Note that the estimated feedback gains $\widetilde{\alpha}_2$ and $\widetilde{\beta}_2$ are significantly smaller than the values deducted from macroscopic data, such as $\alpha \approx 0.6$ [1/s], $\beta \approx 0.9$ [1/s] in Ge et al. (2016). Since the algorithm for $\widetilde{\kappa}_i$ involves division, we present $\widetilde{\kappa}_i$ after filtering the numerical noise using a third-order Savitzky-Golay filter with window size $\frac{1}{3}N\Delta t = 5$ [s]; see Fig. 5(d).

In Fig. 5, the human reaction time, feedback gains, and range policy slope exhibits stochastic variations. While their values can be averaged over time for connected vehicle design, it is desirable to examine their distribution over a larger data set. Therefore, we repeated the experiment shown in Fig. 3 and accumulated over ten thousand estimations for each following vehicle. In particular, we present the distribution of driver parameters for vehicles 2 and 3.

In Fig. 6(a,b) we show the histogram of estimated driver reaction time $\widetilde{\tau}_2$ and $\widetilde{\tau}_3$, respectively. The mean and variance of the driver reaction time for car 2 is (1.16, 0.19) [s], while for car 3 we have (0.89, 0.12) [s]. Although the two drivers have different mean and variance in the reaction time, their distributions are not significantly different from each other. Thus, we may assume a nominal distribution of $\widetilde{\tau}_i$ for both drivers when designing a connected automated vehicle that uses motion information from vehicles 2 and 3.

In Fig. 7 we show the histograms of human feedback gains $\widetilde{\alpha}_i$, $\widetilde{\beta}_i$ and range policy slope $\widetilde{\kappa}_i$ for vehicle 2 (panels (a,c,e)) and vehicle 3 (panels (b,d,f)). By comparing Fig. 7(a,c,e) and (b,d,f) one may observe that, while there exist some differences in each pair of histograms (a,b), (c,d) and (e,f), the range of human feedback gains $\widetilde{\alpha}_i$, $\widetilde{\beta}_i$ and range policy slope $\widetilde{\kappa}_i$ are the same for the two drivers. Thus, one may represent $\widetilde{\alpha}_i$, $\widetilde{\beta}_i$, $\widetilde{\kappa}_i$ of both drivers using a set of nominal distributions in connected automated vehicle design.

5. Optimal connected cruise control design considering human behavior

In this section, we first modify the theoretical car-following model to consider variations in human driver parameters. Then using the data-based car-following model, we design an optimal connected cruise controller that is able to reduce the speed fluctuations of

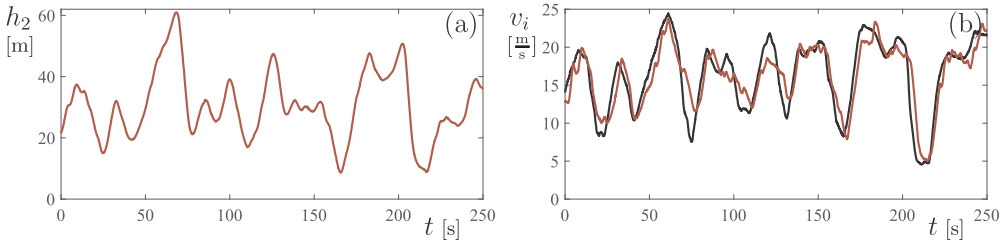

Fig. 4. (a): Headway of vehicle 2 during one test run. (b): Velocity of vehicles 2 (red curve) and 3 (black curve) during one test run. (For interpretation of the references to color in this figure legend, the reader is referred to the web version of this article.)

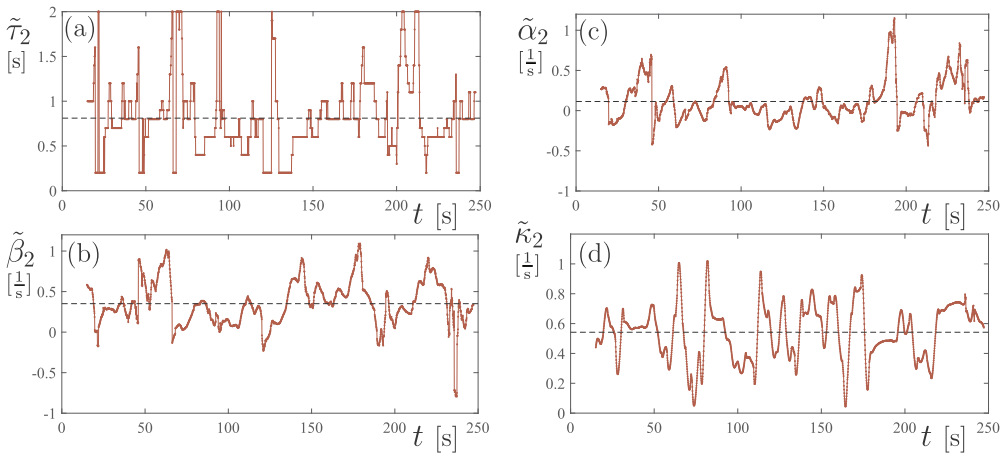

Fig. 5. Estimated driver parameters of vehicle 2 in the test run shown in Fig. 4 starting from $t = 15$ [s]. (a): The time profile of estimated delay time $\widetilde{\tau}_2$ with the quantization step $\Delta t = 0.1$ [s] and the range of [0.2, 2] [s]. (b,c): The time profile of estimated feedback gains $\widetilde{\alpha}_2$, $\widetilde{\beta}_2$. (d): The time profile of estimated range policy slope $\widetilde{\kappa}_2$, filtered by a third-order Savitzky-Golay filter of window size 5 [s]. The dashed black lines denote the mean values.

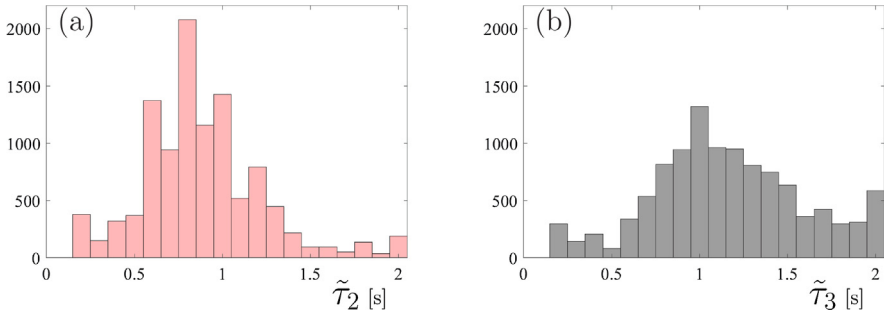

Fig. 6. Histograms of estimated driver reaction time for vehicles 2 and 3.

the CCC vehicle. Finally, the performance of this data-driven connected automated vehicle design is tested using the experimental data.

We consider the scenario shown in Fig. 8 where the vehicle at the tail (dark blue) is a connected automated vehicle. The red arrows indicate feedback terms using the motion information from corresponding vehicles ahead. In this case, only vehicle 1 needs to be longitudinally automated, while all other vehicles only need to be equipped with V2V communication devices.

5.1. Data-driven connected cruise control design

Without the data-driven estimations shown in Section 4, we can only use theoretical car-following models like (4) to design connected cruise controllers. In particular, (Ge and Orosz, 2017) proposed an optimal design that minimizes the spacing and speed fluctuations while penalizing the control efforts. It was shown that with appropriate weighting factors, the CCC vehicle can be theoretically head-to-tail string stable. That is, vehicle 1 has smaller speed fluctuations compared with vehicle 4, the vehicle farthest ahead whose motion signal is used in the connected cruise controller. Here, we modify the car-following model (4) to better describe the motion of human-driven vehicles nearby. Then, by adapting the string-stable optimal design to this data-driven car-following model, we facilitate the implementation of connected cruise control in real traffic.

We consider the mean dynamics of (4) with stochastic parameters $\widetilde{\alpha}_i$, $\widetilde{\beta}_i$, $\widetilde{\kappa}_i$ and $\widetilde{\tau}_i$, cf. Figs. 6 and 7. Under certain assumptions (Gomez et al., 2016; Sadeghpour and Orosz, 2018), we can use the mean values $\overline{\alpha}_i$, $\overline{\beta}_i$, $\overline{\kappa}_i$ to represent stochastic human parameters $\widetilde{\alpha}_i$, $\widetilde{\beta}_i$ and $\widetilde{\kappa}_i$, yet the distribution of driver reaction time $\widetilde{\tau}_i$ cannot be simply represented by its mean value (see Appendix A). Instead, the probability density function of driver reaction time $\widetilde{\tau}_i$ appears explicitly in distributed delay terms. That is, the data-based car-following model for human-driven vehicle i becomes

$$\begin{aligned} \dot{h}_i(t) &= v_{i+1}(t) - v_i(t), \\ \dot{v}_i(t) &= \overline{\alpha}_i \int_{-\tau_{\max}}^{0} w_i(\theta)(\overline{\kappa}_i h_i(t+\theta) - v_i(t+\theta))\,\mathrm{d}\theta + \overline{\beta}_i \int_{-\tau_{\max}}^{0} w_i(\theta)(v_{i+1}(t+\theta) - v_i(t+\theta))\,\mathrm{d}\theta, \end{aligned} \tag{13}$$

where $w_i(\theta)$ is the normed kernel of the distributed delay $\theta \in [-\tau_{\max}, 0]$ due to the distribution of human reaction time $\widetilde{\tau}_i \in [0, \tau_{\max}]$.

On the other hand, the car-following dynamics of the connected automated vehicle is given by

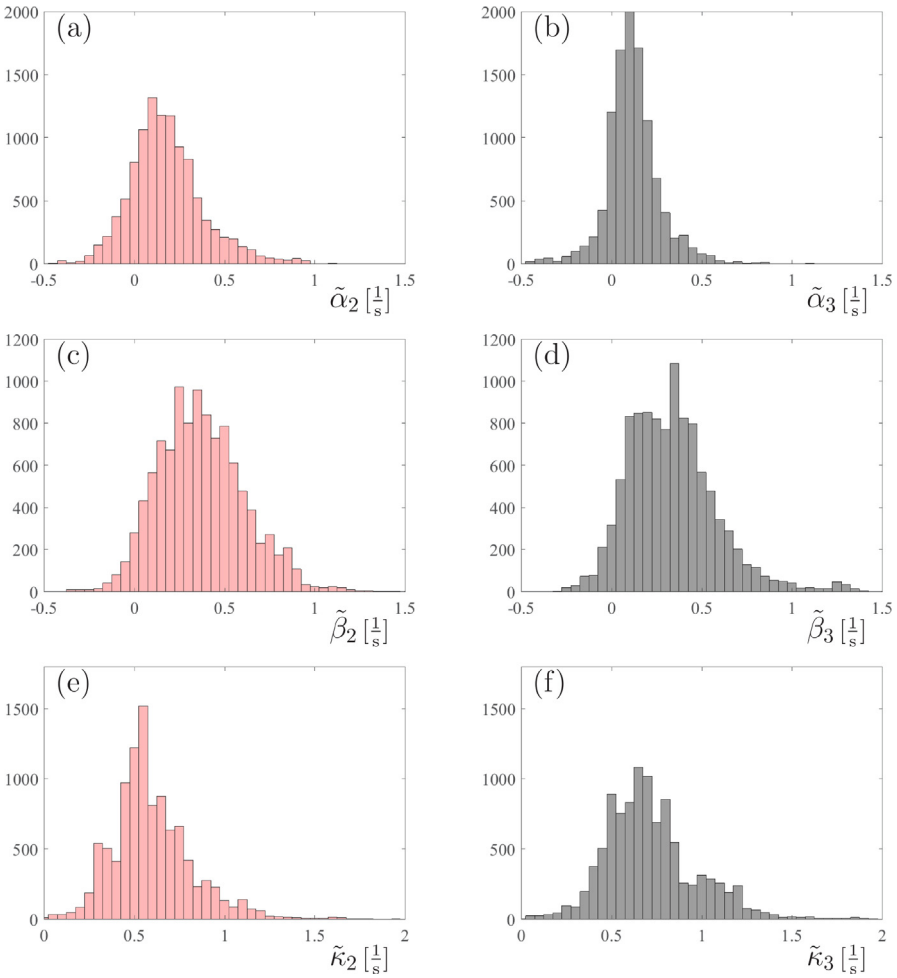

Fig. 7. (a,c,e): Histogram of human feedback gains $\tilde{\alpha}_2$, $\tilde{\beta}_2$ and range policy slope $\tilde{\kappa}_2$ for vehicle 2. (b,d,f): Histogram of human feedback gains $\tilde{\alpha}_3$, $\tilde{\beta}_3$ and range policy slope $\tilde{\kappa}_3$ for vehicle 3.

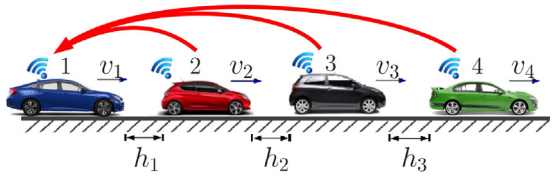

Fig. 8. The connected vehicle system setup: a string of 4 vehicles on a single-lane road where all vehicles are equipped with GPS and V2V communication devices and the last, connected automated vehicle is driven by a CCC algorithm. The red arrows represent feedback terms in the connected cruise controller that use motion information received from vehicles ahead. (For interpretation of the references to color in this figure legend, the reader is referred to the web version of this article.)

$$\begin{aligned} \dot{h}_1(t) &= v_2(t) - v_1(t), \\ \dot{v}_1(t) &= u(t), \end{aligned} \tag{14}$$

where $u(t)$ is the optimal CCC controller to be designed. While (14) does not detail powertrain dynamics nor consider physical effects such as rolling resistance and wind drag, CCC designs based on this model can be implemented in a hierarchical manner, where these effects are compensated by the lower-level controller (Zhang et al., 2018). In order to have feedback terms in $u(t)$ that are similar to those in human car-following behavior (4) and (13), we define

$$x_i = \begin{bmatrix} \overline{\kappa}_i h_i - v_i \\ v_{i+1} - v_i \end{bmatrix}, \quad \phi_n = \begin{bmatrix} 0 \\ \dot{v}_{n+1} \end{bmatrix}, \tag{15}$$

where $i = 1, \ldots, n$. Here we have $n = 3$ (cf. Fig. 8). While larger n is allowed in this framework, the range of reliable vehicle-to-vehicle

communication often impose the limit $n \leqslant 4$.

We construct the state and disturbance vectors

$$X = \begin{bmatrix} x_1 \\ \vdots \\ x_n \end{bmatrix}, \quad \phi = \begin{bmatrix} 0 \\ \vdots \\ 0 \\ \phi_n \end{bmatrix}, \tag{16}$$

and write the dynamics of the connected vehicle system (13), (14) as

$$\dot{X}(t) = \mathbf{A}X(t) + \int_{-\tau_{\max}}^{0} \mathbf{G}(\theta)X(t+\theta)\mathrm{d}\theta + \mathbf{D}u(t) + \phi(t). \tag{17}$$

The coefficient matrices are given by

$$\mathbf{A} = \begin{bmatrix} \mathbf{A}_1 & & \\ & \ddots & \\ & & \mathbf{A}_n \end{bmatrix}, \quad \mathbf{D} = \begin{bmatrix} \mathbf{D}_1 \\ \mathbf{0} \\ \vdots \\ \mathbf{0} \end{bmatrix}, \quad \mathbf{G}(\theta) = \begin{bmatrix} \mathbf{0} & \mathbf{G}_{12}(\theta) & & & \\ & \mathbf{G}_{22}(\theta) & \mathbf{G}_{23}(\theta) & & \\ & & \ddots & \ddots & \\ & & & & \mathbf{G}_{nn}(\theta) \end{bmatrix}, \tag{18}$$

where the blocks are defined by

$$\begin{aligned} &\mathbf{A}_i = \begin{bmatrix} 0 & \overline{\kappa}_i \\ 0 & 0 \end{bmatrix}, \quad \mathbf{B}_{ii} = -\begin{bmatrix} \overline{\alpha}_i & \overline{\beta}_i \\ \overline{\alpha}_i & \overline{\beta}_i \end{bmatrix}, \quad \mathbf{G}_{ii}(\theta) = \mathbf{B}_{ii}w_i(\theta), \\ &\mathbf{D}_1 = \begin{bmatrix} -1 \\ -1 \end{bmatrix}, \quad \mathbf{B}_{(i-1)i} = \begin{bmatrix} 0 & 0 \\ \overline{\alpha}_i & \overline{\beta}_i \end{bmatrix}, \quad \mathbf{G}_{(i-1)i}(\theta) = \mathbf{B}_{(i-1)i}w_i(\theta). \end{aligned} \tag{19}$$

We define the multi-objective cost function for the connected automated vehicle

$$J_{t_f}(u, X) = \int_0^{t_f} (u^2 + \gamma_h(\overline{\kappa}_1 h_1 - v_1)^2 + \gamma_v(v_2 - v_1)^2)\mathrm{d}t = \int_0^{t_f} (u^2 + X^{\mathrm{T}}\Gamma X)\mathrm{d}t, \tag{20}$$

where the weights $\gamma_h > 0$, $\gamma_v > 0$ and $\Gamma = \mathrm{diag}[\gamma_h, \gamma_v, 0, ..., 0] \in \mathbb{R}^{2n\times 2n}$. The optimal controller to (17), (20) is

$$u(t) = -\mathbf{D}^{\mathrm{T}}\left(\mathbf{P}_1(t)X(t) + \int_{-\tau_{\max}}^{0} \mathbf{Q}_1(t, \theta)X(t+\theta)\mathrm{d}\theta + \mathbf{P}_2(t) + \int_{-\tau_{\max}}^{0} \mathbf{Q}_2(t, \theta)\mathrm{d}\theta\right), \tag{21}$$

where the matrices $\mathbf{P}_1(t)$, $\mathbf{Q}_1(t, \theta)$ are not influenced by the disturbance $\phi(t)$.

In Ge and Orosz (2017) we found that a connected cruise controller can be designed with minimal computational cost and satisfactory performance when assuming $\phi(t) = 0$ and infinite time horizon. Since the controller (21) has the same structure as in Ge and Orosz (2017), we assume $\phi(t) = 0$ and $t_f \to \infty$ in (20), which yields the steady-state solution

$$\begin{aligned} &\mathbf{P}_1(t) \equiv \mathbf{P}_1, \quad \mathbf{Q}_1(t, \theta) \equiv \mathbf{Q}_1(\theta), \quad \mathbf{R}_1(t, \xi, \theta) \equiv \mathbf{R}_1(\xi, \theta), \\ &\mathbf{P}_2(t) \equiv \mathbf{0}, \quad \mathbf{Q}_2(t, \theta) \equiv \mathbf{0}. \end{aligned} \tag{22}$$

Substituting (22) into (21) leads to the simplified controller

$$u(t) = -\mathbf{D}^{\mathrm{T}}\left(\mathbf{P}_1X(t) + \int_{-\tau_{\max}}^{0} \mathbf{Q}_1(\theta)X(t+\theta)\mathrm{d}\theta\right), \tag{23}$$

where the matrices $\mathbf{P}_1$, $\mathbf{Q}_1(\theta)$ are given by

$$\begin{aligned} &\mathbf{A}^{\mathrm{T}}\mathbf{P}_1 + \mathbf{P}_1\mathbf{A} - \mathbf{P}_1\mathbf{D}\mathbf{D}^{\mathrm{T}}\mathbf{P}_1 + \mathbf{Q}_1(0) + \mathbf{Q}_1^{\mathrm{T}}(0) + \Gamma = \mathbf{0}, \\ &\partial_\theta\mathbf{Q}_1(\theta) = (\mathbf{A}^{\mathrm{T}} - \mathbf{P}_1\mathbf{D}\mathbf{D}^{\mathrm{T}})\mathbf{Q}_1(\theta) + \mathbf{P}_1\mathbf{G}(\theta) + \mathbf{R}_1(0, \theta), \\ &(\partial_\xi + \partial_\theta)\mathbf{R}_1(\xi, \theta) = \mathbf{G}^{\mathrm{T}}(\xi)\mathbf{Q}_1(\theta) + \mathbf{Q}_1^{\mathrm{T}}(\xi)\mathbf{G}(\theta) - \mathbf{Q}_1^{\mathrm{T}}(\xi)\mathbf{D}\mathbf{D}^{\mathrm{T}}\mathbf{Q}_1(\theta), \end{aligned} \tag{24}$$

with boundary conditions

$$\mathbf{Q}_1(-\tau_{\max}) = \mathbf{0}, \qquad \mathbf{R}_1(-\tau_{\max}, \theta) = \mathbf{0}, \tag{25}$$

see (Kolmanovskii and Myshkis, 1992) for proofs. Since the coefficient matrices $\mathbf{A}$ and $\mathbf{G}(\theta)$ are upper-triangular, we can use the recursive method introduced in Ge and Orosz (2017) to analytically solve this LQ problem with distributed delay.

Solving (24), (25), an analytical solution can be obtained for the optimal CCC controller

$$\begin{aligned} u(t) = &\sum_{i=1}^{n} (\alpha_{1i}(\overline{\kappa}_i h_i(t) - v_i(t)) + \beta_{1i}(v_{i+1}(t) - v_i(t))) \\ &+ \sum_{i=1}^{n} \int_{-\tau_{\max}}^{0} f_i(\theta)(\overline{\kappa}_i h_i(t+\theta) - v_i(t+\theta))\mathrm{d}\theta + \sum_{i=1}^{n} \int_{-\tau_{\max}}^{0} g_i(\theta)(v_{i+1}(t+\theta) - v_i(t+\theta))\mathrm{d}\theta, \end{aligned} \tag{26}$$

where the CCC gains α_{1i}, β_{1i} and kernels $f_i(\theta)$, $g_i(\theta)$ can be calculated using (37), (38), (45), (48), (49), (50), (51) in Appendix B.

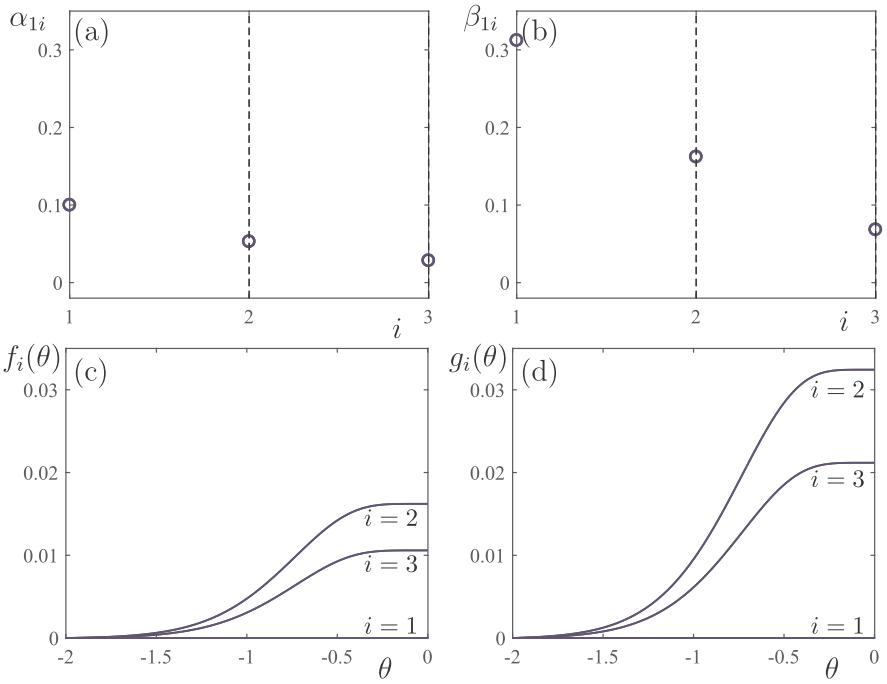

Fig. 9. Optimal feedback gains α_{1i}, β_{1i} and kernels $f_i(\theta)$, $g_i(\theta)$ in the CCC controller (26). We assume that the human reaction time follows Gamma distribution (53) with the mean value 0.86 [s] and the variance 0.30 [s]. The weights in the cost function are $\gamma_h = 0.01$, $\gamma_v = 0.04$.

While all preceding vehicles are human-driven in Fig. 8, the optimal connected cruise control design can be extended to the case when some preceding vehicles are also driven by connected cruise controllers. However, such scenarios are rare when the penetration rate of driving automation is low. Therefore, for this data-driven design, we assume a CCC vehicle does not "look beyond" another CCC vehicle. For example, if vehicle 3 in Fig. 8 is another CCC vehicle, then vehicle 1 would no longer use motion information of vehicle 4. In this way, multiple CCC vehicles in the traffic flow will only generate a cascade of connected vehicle systems where each connected vehicle system only contains one CCC vehicle at the tail.

We also note that the weighting factors γ_h and γ_v in the cost function (20) should be chosen such that the optimal CCC design (26) is string stable. While the string stable regions in the (γ_h, γ_v)-plane can be calculated similarly as in Ge and Orosz (2017), we provide more details in Appendix C. We also note that the optimal CCC controller (26) only contains speed and spacing feedback, while acceleration feedback has been found to improve car-following performance as well (Ge and Orosz, 2014). Since the optimal CCC design can be readily extended to include the acceleration feedback, detailed discussions are omitted here.

5.2. Data-driven evaluation of the connected cruise controller

By replacing the human driver in vehicle 1 with the optimal controller (26), we evaluate the performance of this connected cruise controller using experimental data and compare it with what the human driver has achieved during the tests. While the controller gains and kernels (45), (50), (51) allow heterogeneous human parameters $\overline{\alpha}_i$, $\overline{\beta}_i$, $\overline{\kappa}_i$ and delay distribution $w_i(\theta)$, for simplicity, here we assume the parameters and delay distribution for vehicles 2 and 3 are the same, i.e., $\overline{\alpha}_2 = \overline{\alpha}_3 = 0.2$ [1/s], $\overline{\beta}_2 = \overline{\beta}_3 = 0.4$ [1/s], $\overline{\kappa}_2 = \overline{\kappa}_3 = 0.6$ [1/s]; cf. Fig. 7(b,d,f). We also assume the human reaction time $\widetilde{\tau}_2$ and $\widetilde{\tau}_3$ follow the same Gamma distribution, and obtain its probability density function using the histograms shown in Fig. 6. We also set weights $\gamma_h = 0.01$, $\gamma_v = 0.04$ in the cost function (20).

In Fig. 9, the feedback gains α_{1i}, β_{1i} and kernels $f_i(\theta)$, $g_i(\theta)$ are plotted for Gamma-distributed human reaction time. Fig. 9(a,b) show that the feedback gains decay as vehicle number i increases, i.e., as the motion information comes from vehicles farther downstream. Fig. 9(c,d) show that the kernels $f_1(\theta) = 0$ and $g_1(\theta) = 0$, while the kernels $f_i(\theta)$ and $g_i(\theta)$ for $i > 1$ decrease both as i increases and as θ approaches $-\tau_{max}$. These qualitative features remain the same when the number of preceding vehicles increases, or when Gaussian distribution is assumed for human reaction time.

With feedback gains and kernels given in Fig. 9, we replace the human driver in vehicle 1 with the CCC controller (26) (cf. Figs. 3 and 8), and evaluate the performance of CCC in the same traffic situations that the human driver has experienced. In Fig. 10(a), the spacing of vehicles 3, 2, and 1 observed in an experiment are plotted as black, red, and light blue, respectively, and the dark blue curve is the spacing response of vehicle 1 when it is driven by the CCC algorithm. The CCC algorithm produces much smaller spacing fluctuations (dark blue curve) compared to the human driver. In particular, while the human-driven vehicle 1 almost collided with vehicle 2 in the experiment (light blue curve at $t \approx 210$ [s]), such a safety hazard is avoided when vehicle 1 is driven by the CCC algorithm (dark blue curve at $t \approx 210$ [s]). In Fig. 10(b) the green curve is the velocity v_1 of the head vehicle, while the other curves have the same color scheme as in panel (a). Again, the CCC vehicle at the tail has smaller fluctuations in velocity compared with other

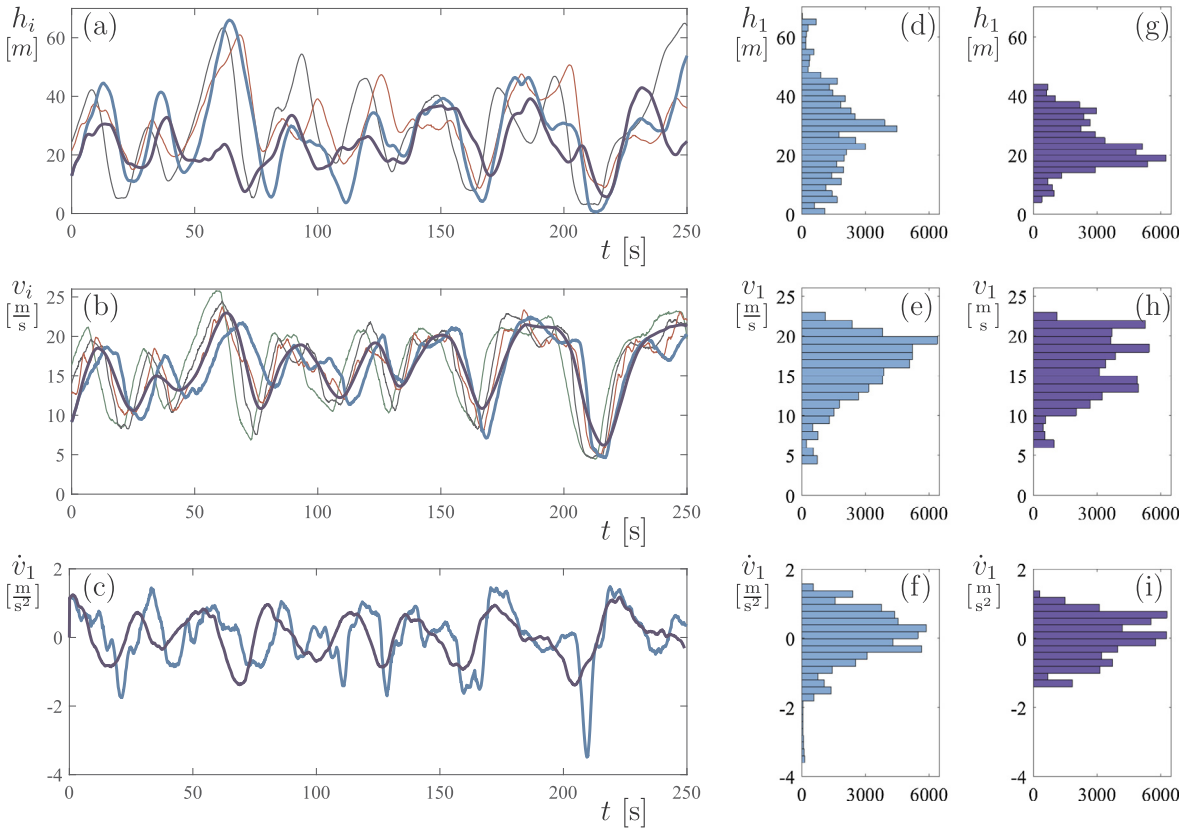

Fig. 10. (a,b,c) The spacing, velocity, and acceleration profiles of a (3 + 1)-car vehicle string. The color scheme is the same as in Fig. 3. The dark blue curves correspond to the connected automated vehicle at the tail that is driven by the CCC controller (26). (d,e,f) The spacing, speed, and acceleration histogram of vehicle 1 when it is human-driven. (g,h,i) The spacing, speed, and acceleration histogram of vehicle 1 when it is connected automated. (For interpretation of the references to color in this figure legend, the reader is referred to the web version of this article.)

vehicles. In Fig. 10(c) we compare the acceleration $\dot{v}_1$ of the tail vehicle when it is human-driven (light blue curve) and when it is driven by the CCC algorithm (dark blue curve). Notice that even though the limits for acceleration and braking are not explicitly included in the optimal control setup (17), (20), the CCC vehicle is able to avoid the harsh braking and acceleration maneuvers.

We also compare the spacing, speed, and acceleration histograms of vehicle 1 when it is driven by a human driver (Fig. 10(d,e,f)) with when it is driven by the CCC algorithm (Fig. 10(g,h,i)). The CCC-driven spacing h_1 has significantly fewer instances when it is above 40 [m] or below 5 [m]; see Fig. 10(d,g). While the CCC speed histogram Fig. 10(h) is slightly improved compared with the human-driven Fig. 10(e), the acceleration histogram Fig. 10(i) has much fewer harsh braking instances compared with Fig. 10(f). In particular, the CCC-driven vehicle 1 has no instances when it brakes more than -1.5 [m/s^2]. Therefore, we conclude that the CCC controller demonstrates significant performance improvements compared with the human-driven vehicle.

6. Conclusion

In this paper we first designed an estimation algorithm for a connected automated vehicle to identify the dynamics of preceding vehicles via vehicle-to-vehicle communication. This algorithm can be implemented in real time, and is able to cope with time-varying human parameters. Both characteristics are crucial for application in connected automated vehicle design. Based on experiments on public roads we saw that human parameters are time-varying, and appear to follow certain distributions. While the distributions vary between different drivers, a nominal set of distributions may be assumed for connected automated vehicle design. Then we designed a connected cruise controller using the mean values of human gains and the distribution function of human reaction time. The optimal CCC controller is tested using spacing and velocity data collected in a four-car experiment, and it is shown to reject traffic disturbances much better than a human driver. In the future, more experiments will be conducted under different driving conditions to further understand human car-following behaviors, and data-driven methods will be exploited to describe a richer set of human driving behaviors for better connected automated vehicle design.

Acknowledgment

The authors thank Professor A. Galip Ulsoy for the very insightful discussions and the Commsignia, Inc. for the technical supports. This research has been supported by the Mobility Transformation Center of the University of Michigan.

Appendix A

We consider the linearized human car-following model (4) with stochastic variations in the human feedback gains α_i, β_i, range policy function slope κ_i and reaction time τ_i (see Figs. 6 and 7) and take the expected value

$$\begin{aligned}&\mathbb{E}[\dot{h}_i(t)] = \mathbb{E}[v_{i+1}(t)]-\mathbb{E}[v_i(t)],\\&\mathbb{E}[\dot{v}_i(t)] = \mathbb{E}[\alpha_i(t)(\kappa_i(t)h_i(t-\tau_i(t))-v_i(t-\tau_i(t)))] + \mathbb{E}[\beta_i(t)(v_{i+1}(t-\tau_i(t))-v_i(t-\tau_i(t)))].\end{aligned} \tag{27}$$

We denote the state variables and parameters

$$\overline{h}_i(t) = \mathbb{E}[h_i(t)], \quad \overline{v}_i(t) = \mathbb{E}[v_i(t)], \quad \overline{\alpha}_i = \mathbb{E}[\alpha_i(t)], \quad \overline{\beta}_i = \mathbb{E}[\beta_i(t)], \quad \overline{\kappa_i} = \mathbb{E}[\kappa_i(t)], \tag{28}$$

and assume there exist independent and stationary distributions of the parameters α_i, β_i, κ_i and τ_i and their autocorrelation functions decay fast. Then (27) can be simplified as

$$\begin{aligned}&\dot{\overline{h}}_i(t) = \overline{v}_{i+1}(t)-\overline{v}_i(t),\\&\dot{\overline{v}}_i(t) = \overline{\alpha}_i(\overline{\kappa}_i\mathbb{E}[h_i(t-\tau_i(t))]-\mathbb{E}[v_i(t-\tau_i(t))]) + \overline{\beta}_i(\mathbb{E}[v_{i+1}(t-\tau_i(t))]-\mathbb{E}[v_i(t-\tau_i(t))]).\end{aligned} \tag{29}$$

We assume

$$\mathbb{E}[v_i(t-\tau_i(t))] = \int_0^{\tau_{\max}} \overline{v}_i(t-\tau_i)w_i(\tau_i)\mathrm{d}\tau_i, \tag{30}$$

where $\tau_{\max}$ is the maximum human driver reaction time, and $w_i(\tau_i)$ is the probability density function of $\tau_i(t) \in [0,\ \tau_{\max}]$; see (Gomez et al., 2016) for more details behind this assumption. Then we have

$$\begin{aligned}&\dot{\overline{h}}_i(t) = \overline{v}_{i+1}(t)-\overline{v}_i(t),\\&\dot{\overline{v}}_i(t) = \overline{\alpha}_i\int_{-\tau_{\max}}^0 w_i(\theta)(\overline{\kappa}_i\overline{h}_i(t+\theta)-\overline{v}_i(t+\theta))\mathrm{d}\theta + \overline{\beta}_i\int_{-\tau_{\max}}^0 w_i(\theta)(\overline{v}_{i+1}(t+\theta)-\overline{v}_i(t+\theta))\mathrm{d}\theta,\end{aligned} \tag{31}$$

where $w_i(\theta)$ is the probability density function of the delay $\theta \in [-\tau_{\max},\ 0]$. In this way, we modify (4) so that it contains the expected values of the human gains and the distribution of human driver reaction time. In (13), the bars above h_i and v_i are dropped for simplicity.

Appendix B

In order to solve (24), (25), we denote

$$\mathbf{P}_1 = \begin{bmatrix}\mathbf{P}_{11} & \cdots & \mathbf{P}_{1n}\\ \vdots & \ddots & \vdots\\ \mathbf{P}_{n1} & \cdots & \mathbf{P}_{nn}\end{bmatrix}, \quad \mathbf{Q}_1(\theta) = \begin{bmatrix}\mathbf{Q}_{11}(\theta) & \cdots & \mathbf{Q}_{1n}(\theta)\\ \vdots & \ddots & \vdots\\ \mathbf{Q}_{n1}(\theta) & \cdots & \mathbf{Q}_{nn}(\theta)\end{bmatrix}, \tag{32}$$

where $\mathbf{P}_{ij}$, $\mathbf{Q}_{ij}(\theta) \in \mathbb{R}^{2\times 2}$ for $i, j = 1,\ ...,n$, and the CCC controller (23) becomes

$$u(t) = -\mathbf{D}_1^{\mathrm{T}}\sum_{i=1}^{n}\left(\mathbf{P}_{1i}x_i(t) + \int_{-\tau_{\max}}^0 \mathbf{Q}_{1i}(\theta)x_i(t+\theta)\mathrm{d}\theta\right), \tag{33}$$

where $x_i(t)$ is defined in (15). Note that we only need to derive $\mathbf{P}_{1i}$, $\mathbf{Q}_{1i}(\theta)$ for $i = 1,\ ...,n$ to construct the controller, cf. (18), (19). Substituting (32) into (24), (25), we obtain equations for each block $\mathbf{P}_{ij}$, $\mathbf{Q}_{ij}(\theta)$, $\mathbf{R}_{ij}(\xi,\ \theta)$ for $i, j = 1,\ ...,n$, and then solve them recursively.

To start with, $\mathbf{P}_{11}$ and $\mathbf{Q}_{11}(\theta)$ are given by

$$\begin{aligned}&\widehat{\mathbf{A}}_1\mathbf{P}_{11} + \mathbf{P}_{11}\mathbf{A}_1 + \mathbf{Q}_{11}(0) + \mathbf{Q}_{11}^{\mathrm{T}}(0) + \mathrm{diag}[\gamma_{\mathrm{h}},\ \gamma_{\mathrm{v}}] = \mathbf{0},\\&\partial_\theta\mathbf{Q}_{11}(\theta) = \widehat{\mathbf{A}}_1\mathbf{Q}_{11}(\theta) + \mathbf{R}_{11}(0,\ \theta),\\&(\partial_\xi + \partial_\theta)\mathbf{R}_{11}(\xi,\ \theta) = -\mathbf{Q}_{11}^{\mathrm{T}}(\xi)\mathbf{D}\mathbf{D}^{\mathrm{T}}\mathbf{Q}_{11}(\theta),\end{aligned} \tag{34}$$

with boundary conditions

$$\mathbf{Q}_{11}(-\tau_{\max}) = \mathbf{0}, \qquad \mathbf{R}_{11}(-\tau_{\max},\ \theta) = \mathbf{0}, \tag{35}$$

where

$$\widehat{\mathbf{A}}_1 = \mathbf{A}_1^{\mathrm{T}}-\mathbf{P}_{11}\mathbf{D}_1\mathbf{D}_1^{\mathrm{T}}. \tag{36}$$

The solution of (34), (35) is

$$\mathbf{P}_{11} = \begin{bmatrix} p_{11} & p_{12} \\ p_{12} & p_{22} \end{bmatrix}, \quad \mathbf{Q}_{11}(\theta) \equiv \mathbf{0}, \quad \mathbf{R}_{11}(\xi, \theta) \equiv \mathbf{0}, \tag{37}$$

where

$$\begin{aligned} p_{11} &= \frac{-\gamma_\mathrm{h} + \sqrt{\gamma_\mathrm{h}}\sqrt{\gamma_\mathrm{h} + \gamma_\mathrm{v} + 2\overline{\kappa}_1\sqrt{\gamma_\mathrm{h}}}}{\overline{\kappa}_1}, \\ p_{12} &= \sqrt{\gamma_\mathrm{h}} - p_{11}, \\ p_{22} &= -2\sqrt{\gamma_\mathrm{h}} + \sqrt{\gamma_\mathrm{h} + \gamma_\mathrm{v} + 2\overline{\kappa}_1\sqrt{\gamma_\mathrm{h}}} + p_{11}, \end{aligned} \tag{38}$$

which is the only solution satisfying the condition $\mathbf{P}_{11} > \mathbf{0}$. Notice that the matrix $\mathbf{P}_{11}$ only depends on the weights γ_h, γ_v and the CCC vehicle's range policy slope $\overline{\kappa}_1$.

Then, to obtain $\mathbf{P}_{1i}$, $\mathbf{Q}_{1i}(\theta)$, $\mathbf{Q}_{i1}(\theta)$ for $i = 2, \ldots, n$, we need to solve

$$\begin{aligned} &\widehat{\mathbf{A}}_1\mathbf{P}_{1i} + \mathbf{P}_{1i}\mathbf{A}_i + \mathbf{Q}_{1i}(0) + \mathbf{Q}_{i1}^\mathrm{T}(0) = \mathbf{0}, \\ &\partial_\theta \mathbf{Q}_{1i}(\theta) = \widehat{\mathbf{A}}_1\mathbf{Q}_{1i}(\theta) + \mathbf{P}_{1(i-1)}\mathbf{G}_{(i-1)i}(\theta) + \mathbf{P}_{1i}\mathbf{G}_{ii}(\theta) + \mathbf{R}_{1i}(0, \theta), \\ &\partial_\theta \mathbf{Q}_{i1}(\theta) = \mathbf{A}_1^\mathrm{T}\mathbf{Q}_{i1}(\theta) - \mathbf{P}_{1i}^\mathrm{T}\mathbf{D}_1\mathbf{D}_1^\mathrm{T}\mathbf{Q}_{11}(\theta) + \mathbf{R}_{1i}^\mathrm{T}(\theta, 0), \\ &(\partial_\xi + \partial_\theta)\mathbf{R}_{1i}(\xi, \theta) = \mathbf{Q}_{(i-1)1}^\mathrm{T}(\theta)\mathbf{G}_{(i-1)i} + \mathbf{Q}_{i1}^\mathrm{T}(\theta)\mathbf{G}_{ii} - \mathbf{Q}_{11}^\mathrm{T}(\xi)\mathbf{D}_1\mathbf{D}_1^\mathrm{T}\mathbf{Q}_{1i}(\theta), \end{aligned} \tag{39}$$

with boundary conditions

$$\begin{aligned} &\mathbf{Q}_{1i}(-\tau_{\max}) = \mathbf{0}, \quad \mathbf{Q}_{i1}(-\tau_{\max}) = \mathbf{0}, \\ &\mathbf{R}_{1i}(\theta, -\tau_{\max}) = \mathbf{0}, \quad \mathbf{R}_{1i}(-\tau_{\max}, \theta) = \mathbf{0}. \end{aligned} \tag{40}$$

Now (39), (40) give the solution

$$\mathbf{Q}_{i1}(\theta) \equiv \mathbf{0}, \quad \mathbf{R}_{1i}(\xi, \theta) \equiv \mathbf{0}, \tag{41}$$

while the equations for $\mathbf{Q}_{1i}(\theta)$ simplify to

$$\begin{aligned} &\partial_\theta \mathbf{Q}_{1i}(\theta) = \widehat{\mathbf{A}}_1\mathbf{Q}_{1i}(\theta) + \mathbf{P}_{1(i-1)}\mathbf{G}_{(i-1)i}(\theta) + \mathbf{P}_{1i}\mathbf{G}_{ii}(\theta), \\ &\mathbf{Q}_{1i}(-\tau_{\max}) = \mathbf{0}, \end{aligned} \tag{42}$$

yielding the solution

$$\mathbf{Q}_{1i}(\theta) = \int_{-\tau_{\max}}^{\theta} \mathrm{e}^{\widehat{\mathbf{A}}_1(\theta-\rho)}(\mathbf{P}_{1(i-1)}\mathbf{G}_{(i-1)i}(\rho) + \mathbf{P}_{1i}\mathbf{G}_{ii}(\rho))\,\mathrm{d}\rho, \tag{43}$$

for $i = 2, \ldots, n$. Thus, the equation for $\mathbf{P}_{1i}$ becomes

$$\int_{-\tau_{\max}}^{0} \mathrm{e}^{-\rho\widehat{\mathbf{A}}_1}(\mathbf{P}_{1(i-1)}\mathbf{G}_{(i-1)i}(\rho) + \mathbf{P}_{1i}\mathbf{G}_{ii}(\rho))\,\mathrm{d}\rho + \widehat{\mathbf{A}}_1\mathbf{P}_{1i} + \mathbf{P}_{1i}\mathbf{A}_i = \mathbf{0}. \tag{44}$$

Applying this recursively yields the solution

$$\mathrm{vec}(\mathbf{P}_{1i}) = \prod_{j=2}^{i} \mathbf{M}_j \mathrm{vec}(\mathbf{P}_{11}), \tag{45}$$

for $i = 2, \ldots, n$. Here $\mathrm{vec}(\cdot)$ gives a column vector by stacking the columns of the matrix on the top of each other, and $\mathbf{M}_i \in \mathbb{R}^{4\times4}$ is given by

$$\mathbf{M}_i = -\left(\mathbf{I} \otimes \widehat{\mathbf{A}}_1 + \mathbf{A}_i^\mathrm{T} \otimes \mathbf{I} + \int_{-\tau_{\max}}^{0} \mathbf{G}_{ii}^\mathrm{T}(\rho) \otimes \mathrm{e}^{-\rho\widehat{\mathbf{A}}_1}\,\mathrm{d}\rho\right)^{-1}\left(\int_{-\tau_{\max}}^{0} \mathbf{G}_{(i-1)i}^\mathrm{T} \otimes \mathrm{e}^{-\rho\widehat{\mathbf{A}}_1}\,\mathrm{d}\rho\right). \tag{46}$$

We recall (18), (19), and note that

$$\int_{-\tau_{\max}}^{0} \mathbf{G}_{ii}^\mathrm{T}(\rho) \otimes \mathrm{e}^{-\rho\widehat{\mathbf{A}}_1}\,\mathrm{d}\rho = \mathbf{B}_{ii}^\mathrm{T} \otimes \left(\mathbf{K}\int_{-\tau_{\max}}^{0} w_i(\rho)\mathrm{e}^{-\rho\widehat{\mathbf{J}}_1}\,\mathrm{d}\rho\,\mathbf{K}^{-1}\right), \tag{47}$$

where $\widehat{\mathbf{J}}_1$ is the Jordan form of $\widehat{\mathbf{A}}_1$ and $\mathbf{K}$ the corresponding transformation matrix. For simplicity, we assume that $\widehat{\mathbf{A}}_1$ has a trivial Jordan form. Then (46) becomes

$$\mathbf{M}_i = -(\mathbf{I} \otimes \widehat{\mathbf{A}}_1 + \mathbf{A}_i^\mathrm{T} \otimes \mathbf{I} + \mathbf{B}_{ii}^\mathrm{T} \otimes (\mathbf{K}\mathbf{L}_i(0)\mathbf{K}^{-1}))^{-1}(\mathbf{B}_{(i-1)i}^\mathrm{T} \otimes (\mathbf{K}\mathbf{L}_i(0)\mathbf{K}^{-1})), \tag{48}$$

with

$$\mathbf{L}_i(\theta) = \begin{bmatrix} l_{i1}(\theta) & 0 \\ 0 & l_{i2}(\theta) \end{bmatrix}, \quad l_{i1}(\theta) = \int_{-\tau_{\max}}^{\theta} w_i(\rho)\mathrm{e}^{-\rho\lambda_1}\,\mathrm{d}\rho, \quad l_{i2}(\theta) = \int_{-\tau_{\max}}^{\theta} w_i(\rho)\mathrm{e}^{-\rho\lambda_2}\,\mathrm{d}\rho, \tag{49}$$

where λ_1 and λ_2 are eigenvalues of $\widehat{\mathbf{A}}_1$ and the diagonal elements of $\widehat{\mathbf{J}}_1$.

Similarly (43) simplifies to

$$\mathbf{Q}_{1i}(\theta) = \mathbf{K}\mathrm{e}^{\theta\hat{\mathbf{J}}_1}\mathbf{L}_i(\theta)\mathbf{K}^{-1}(\mathbf{P}_{1(i-1)}\mathbf{B}_{(i-1)i} + \mathbf{P}_{1i}\mathbf{B}_{ii}). \tag{50}$$

With (37), (38), (45), (48), (49), (50), we have the analytical expression for $\mathbf{P}_{1i}$ and $\mathbf{Q}_{1i}(\theta)$. Recalling the controller (23), we have the CCC gains and kernels

$$[\alpha_{1i} \quad \beta_{1i}] = [1 \quad 1]\mathbf{P}_{1i}, \quad [f_i(\theta) \quad g_i(\theta)] = [1 \quad 1]\mathbf{Q}_{1i}(\theta), \tag{51}$$

where $i = 1, \ldots, n$, $\theta \in [-\tau_{\max}, 0]$. We note that the CCC kernels take the form

$$\begin{aligned} f_i(\theta) &= (a_{i0} + a_{i1}\theta)\mathrm{e}^{\lambda_1\theta}l_{i1}(\theta) + a_{i2}\mathrm{e}^{\lambda_2\theta}l_{i2}(\theta), \\ g_i(\theta) &= (b_{i0} + b_{i1}\theta)\mathrm{e}^{\lambda_1\theta}l_{i1}(\theta) + b_{i2}\mathrm{e}^{\lambda_2\theta}l_{i2}(\theta), \end{aligned} \tag{52}$$

and the coefficients a_{i0}, a_{i1}, a_{i2}, and b_{i0}, b_{i1}, b_{i2} can be calculated using the same procedure as in Ge and Orosz (2017). Here we provide a calculation of $l_{i1}(\theta)$, $l_{i2}(\theta)$ under the assumption that the driver reaction time follows Gamma distribution

$$w_i(\tau_i) = \frac{\tau_i^{a_i-1}\mathrm{e}^{-\tau_i/b_i}}{\int_0^{\tau_{\max}} s^{a_i-1}\mathrm{e}^{-s/b_i}\mathrm{d}s}, \tag{53}$$

where $\tau_i \in [0, \tau_{\max}]$, a_i is the shape parameter and b_i is the scale parameter. Thus, using $\theta \in [-\tau_{\max}, 0]$ we have

$$l_{ij}(\theta) = \frac{\Gamma(a_i, \tau_{\max}/b_i - \lambda_j\tau_{\max}) - \Gamma(a_i, -\theta/b_i + \lambda_j\theta)}{(1-\lambda_j b_i)^{a_i}\Gamma(a_i, \tau_{\max}/b_i)}. \tag{54}$$

for $j = 1, 2$, where $\Gamma(a, b) = \int_0^b t^{a-1}\mathrm{e}^{-t}\mathrm{d}t$ is the lower incomplete Gamma function.

Appendix C

Here we discuss how to tune the weighting factors γ_{h} and γ_{v} to ensure that the optimal CCC design (26) responds well to speed perturbations ahead; see Fig. 8. In particular, we require the optimal controller to be head-to-tail string stable (Zhang and Orosz, 2016). That is, when the motion of human-driven vehicles 2, ..., n oscillates around the steady state (3), the connected automated vehicle should have smaller speed fluctuations compared with vehicle n, the farthest vehicle ahead whose motion information is used. Most human drivers are unable to suppress speed fluctuations propagating through vehicles due to large reaction time (Orosz, 2016). Therefore, speed fluctuations at vehicle 2 is very likely to be more severe than at vehicle n. However, using motion information from vehicles farther ahead, the connected automated vehicle may be able to regulate its speed fluctuations to the same level or even less than at vehicle n.

Recall the dynamics of the connected automated vehicle (14), (26) and human-driven vehicles (13). For vehicle $i = 1, \ldots, n$ in Fig. 8 (where $n = 3$), we define the corresponding spacing and speed perturbations

$$\widetilde{h}_i(t) = h_i(t) - h_i^*, \quad \widetilde{v}_i(t) = v_i(t) - v^*, \tag{55}$$

and obtain the linearized dynamics for the connected automated vehicle and its predecessors as

$$\begin{aligned} \dot{\widetilde{h}}_1(t) &= \widetilde{v}_2(t) - \widetilde{v}_1(t), \\ \dot{\widetilde{v}}_1(t) &= \sum_{i=1}^{n} (\alpha_{1i}(\overline{\kappa}_i\widetilde{h}_i(t) - \widetilde{v}_i(t)) + \beta_{1i}(\widetilde{v}_{i+1}(t) - \widetilde{v}_i(t))) \\ &\quad + \sum_{i=1}^{n} \int_{-\tau_{\max}}^{0} f_i(\theta)(\overline{\kappa}_i\widetilde{h}_i(t+\theta) - \widetilde{v}_i(t+\theta))\mathrm{d}\theta + \sum_{i=1}^{n} \int_{-\tau_{\max}}^{0} g_i(\theta)(\widetilde{v}_{i+1}(t+\theta) - \widetilde{v}_i(t+\theta))\mathrm{d}\theta, \\ \dot{\widetilde{h}}_i(t) &= \widetilde{v}_{i+1}(t) - \widetilde{v}_i(t), \\ \dot{\widetilde{v}}_i(t) &= \overline{\alpha}_i \int_{-\tau_{\max}}^{0} w_i(\theta)(\overline{\kappa}_i\widetilde{h}_i(t+\theta) - \widetilde{v}_i(t+\theta))\mathrm{d}\theta + \overline{\beta}_i \int_{-\tau_{\max}}^{0} w_i(\theta)(\widetilde{v}_{i+1}(t+\theta) - \widetilde{v}_i(t+\theta))\mathrm{d}\theta, \end{aligned} \tag{56}$$

where $i = 2, \ldots, n$. In (56), we consider the speed perturbation $\widetilde{v}_{n+1}$ of the farthest vehicle ahead as the input, and the speed perturbation $\widetilde{v}_1$ of the connected automated vehicle as the output. Then the head-to-tail transfer function is given by

$$H_{\mathrm{H2T}} = \frac{\widetilde{V}_1(s)}{\widetilde{V}_{n+1}(s)} = \frac{\sum_{j=2}^{n+1} H_{j1}(s) \prod_{i=j}^{n} H_{(i+1)i}(s)}{s^2 + (\alpha_{11} + F_1(s) + \beta_{11} + G_1(s))s + (\alpha_{11} + F_1(s))\overline{\kappa}_1}, \tag{57}$$

where $\widetilde{V}_i(s) = \mathscr{L}(\widetilde{v}_i(t))$ denotes the Laplace transform of the speed perturbation $\widetilde{v}_i(t)$. In (57), the pairwise transfer function between human-driven vehicle i and its predecessor (vehicle $i + 1$) is

$$H_{(i+1)i} = \frac{\overline{\alpha}_i\overline{\kappa}_i + \overline{\beta}_i s}{s^2/W_i(s) + (\overline{\alpha}_i + \overline{\beta}_i)s + \overline{\alpha}_i\overline{\kappa}_i}, \tag{58}$$

for $i = 2, \ldots, n$. The transfer link from vehicle j to the connected automated vehicle is

$$H_{j1} = (\alpha_{1(j-1)} + F_{j-1}(s))\overline{\kappa}_{j-1} - (\alpha_{1j} + F_j(s))\overline{\kappa}_j + (\beta_{1(j-1)} + G_{j-1}(s) - \alpha_{1j} - F_j(s) - \beta_{1j} - G_j(s))s, \tag{59}$$

for $j = 2, \ldots, n$, and

$$H_{(n+1)1} = (\alpha_{1n} + F_n(s))\overline{\kappa}_n + (\beta_{1n} + G_n(s))s, \tag{60}$$

with $W_i(s)$, $F_i(s)$ and $G_i(s)$ given by

$$\begin{aligned} W_i(s) &= \int_{-\tau_{\max}}^{0} w_i(\theta) e^{s\theta}\, \mathrm{d}\theta, \quad i = 2, \ldots, n, \\ F_i(s) &= \int_{-\tau_{\max}}^{0} f_i(\theta) e^{s\theta}\, \mathrm{d}\theta,\ G_i(s) = \int_{-\tau_{\max}}^{0} g_i(\theta) e^{s\theta}\, \mathrm{d}\theta, \quad i = 1, \ldots, n. \end{aligned} \tag{61}$$

At the linear level, the criterion for head-to-tail string stability is the amplitude of head-to-tail transfer function (57) being smaller than one for all positive frequencies, that is,

$$|H_{\mathrm{H2T}}(\mathrm{i}\omega)| < 1, \tag{62}$$

for all $\omega > 0$. Note that given the feedback gains $\overline{\alpha}_i$, $\overline{\beta}_i$, range policy gradient $\overline{\kappa}_i$ and delay distribution $w_i(\theta)$ of human driven vehicles, the feedback gains α_{1i}, β_{1i} and kernels $f_i(\theta)$, $g_i(\theta)$ in the optimal controller (26) depend on the design parameters γ_{h}, γ_{v}.

To demonstrate the influence of the design parameters γ_{h}, γ_{v} on the head-to-tail string stability, we consider the scenario when the parameters of vehicles 2 and 3 are the same, i.e., $\overline{\alpha}_2 = \overline{\alpha}_3 = 0.2$ [1/s], $\overline{\beta}_2 = \overline{\beta}_3 = 0.4$ [1/s], $\overline{\kappa}_2 = \overline{\kappa}_3 = 0.6$ [1/s]; cf. Fig. 7(b,d,f). We also assume the human reaction time $\widetilde{\tau}_2$ and $\widetilde{\tau}_3$ follow the same Gamma distribution (53) with parameter $a_2 = a_3 = 6.08$, $b_2 = b_3 = 0.15$; cf. Fig. 6. Based on the optimal controller calculation (37), (38), (45), (48)–(51) and the transfer function formulation (57)–(61), we obtain and plot the string stable region (shaded) in the $(\gamma_{\mathrm{h}}, \gamma_{\mathrm{v}})$-plane in Fig. 11(a).

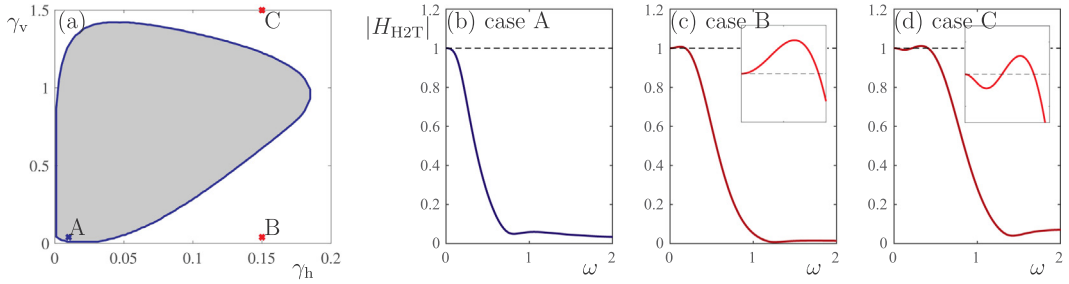

Fig. 11. (a) Head-to-tail string stable region in the $(\gamma_{\mathrm{h}}, \gamma_{\mathrm{v}})$-plane assuming human gains $\overline{\alpha}_2 = \overline{\alpha}_3 = 0.2$ [1/s], $\overline{\beta}_2 = \overline{\beta}_3 = 0.4$ [1/s], $\overline{\kappa}_2 = \overline{\kappa}_3 = 0.6$ [1/s] and reaction time delay (53) with parameter $a_2 = a_3 = 6.08$, $b_2 = b_3 = 0.15$. (b-d) Bode plots at case A ($\gamma_{\mathrm{h}} = 0.01$, $\gamma_{\mathrm{v}} = 0.04$), case B ($\gamma_{\mathrm{h}} = 0.15$, $\gamma_{\mathrm{v}} = 0.04$), and case C ($\gamma_{\mathrm{h}} = 0.15$, $\gamma_{\mathrm{v}} = 1.50$).

To illustrate the string stable criterion (62), we mark a string-stable case ($\gamma_{\mathrm{h}} = 0.01$, $\gamma_{\mathrm{v}} = 0.04$), and two string-unstable cases ($\gamma_{\mathrm{h}} = 0.15$, $\gamma_{\mathrm{v}} = 0.04$, and $\gamma_{\mathrm{h}} = 0.15$, $\gamma_{\mathrm{v}} = 1.50$) in Fig. 11(a), and plot their corresponding amplification ratios against the frequency ω. As demonstrated by case A, choosing the design parameters from the shaded region ensures attenuated speed variations for all frequencies. However, when the design parameters are not in the string-stable region, the connected automated vehicle will not be able to attenuate speed variations at certain frequencies. For example, an optimal CCC design at case B will amplify speed variations at low frequencies, while the design at case C will amplify speed variations in a higher frequency range.

References

Avedisov, S.S., Orosz, G., 2017. Analysis of connected vehicle networks using network-based perturbation techniques. Nonlinear Dyn. 89 (3), 1651–1672.
Barber, P., Engelman, G., King, P., Richardson, M., 2009. Adaptive cruise control system and methodology, including control of inter-vehicle spacing. EP Patent 1,008, 482.
Chen, N., Wang, M., Alkim, T., van Arem, B., 2018. A robust longitudinal control strategy of platoons under model uncertainties and time delays. J. Adv. Transport. 2018, 1–13.
di Bernardo, M., Salvi, A., Santini, S., 2015. Distributed consensus strategy for platooning of vehicles in the presence of time varying heterogeneous communication delays. IEEE Trans. Intell. Transport. Syst. 16 (1), 102–112.
Diop, S., Kolmanovsky, I., Moraal, P., Nieuwstadt, M.V., 2001. Preserving stability/performance when facing an unknown time-delay. Control Eng. Practice 9 (12), 1319–1325.
Drakunov, S., Perruquetti, W., Richard, J.-P., Belkoura, L., 2006. Delay identification in time-delay systems using variable structure observers. Ann. Rev. Control 30 (2), 143–158.
Englund, C., Chen, L., Ploeg, J., Semsar-Kazerooni, E., Voronov, A., Bengtsson, H.H., Didoff, J., 2016. The grand cooperative driving challenge 2016: boosting the introduction of cooperative automated vehicles. IEEE Wireless Commun. 23 (4), 146–152.
Fountoulakis, M., Bekiaris-Liberis, N., Roncoli, C., Papamichail, I., Papageorgiou, M., 2017. Highway traffic state estimation with mixed connected and conventional vehicles: Microscopic simulation-based testing. Transp. Res. Part C 78, 13–33.
Ge, J.I., Avedisov, S.S., He, C.R., Qin, W.B., Sadeghpour, M., Orosz, G., 2018. Experimental validation of connected automated vehicle design among human-driven vehicles. Transp. Res. Part C 91, 335–352.

Ge, J.I., Orosz, G., 2014. Dynamics of connected vehicle systems with delayed acceleration feedback. Transp. Res. Part C 46, 46–64.
Ge, J.I., Orosz, G., 2016. Estimation of feedback gains and delays in connected vehicle systems. In: Proceedings of the American Control Conference. IEEE, pp. 6000–6005.
Ge, J.I., Orosz, G., 2017. Optimal control of connected vehicle systems with communication delay and driver reaction time. IEEE Trans. Intell. Transport. Syst. 18 (8), 2056–2070.
Ge, J.I., Orosz, G., Hajdu, D., Insperger, T., Moehlis, J., 2016. To delay or not to delay – stability of connected cruise control. In: In: Orosz, G., Ersal, T., Insperger, T. (Eds.), Time Delay Systems – Theory, Numerics, Applications and Experiments, Advances in Delays and Dynamics, vol. 7. Springer, pp. 263–282.
Gomez, M.M., Sadeghpour, M., Bennett, M.R., Orosz, G., Murray, R.M., 2016. Stability of systems with stochastic delays and applications to genetic regulatory networks. SIAM J. Appl. Dyn. Syst. 15 (4), 1844–1873.
Gomez, O., Orlov, Y., Kolmanovsky, I.V., 2007. On-line identification of SISO linear time-invariant delay systems from output measurements. Automatica 43 (12), 2060–2069.
Helbing, D., 2001. Traffic and related self-driven many-particle systems. Rev. Mod. Phys. 73, 1067–1141.
Inman, J., 1835. Navigation and Nautical Astronomy: For the Use of British Seamen. C.W. Woodward and J. Rivington.
Jiang, H., Hu, J., An, S., Wang, M., Park, B.B., 2017. Eco approaching at an isolated signalized intersection under partially connected and automated vehicles environment. Transp. Res. Part C 79, 290–307.
Kolmanovskii, V., Myshkis, A., 1992. Applied Theory of Functional Differential Equations. Kluwer Academic Publisher.
Labuhn, P., Chundrlik, W., 1995. Adaptive cruise control. US Patent 5,454,442.
Li, S., Yang, L., Gao, Z., 2015. Coordinated cruise control for high-speed train movements based on a multi-agent model. Transp. Res. Part C 56, 281–292.
Li, S.E., Guo, Q., Xin, L., Cheng, B., Li, K., 2017a. Fuel-saving servo-loop control for adaptive cruise control system of road vehicles with step-gear transmission. IEEE Trans. Vehicul. Technol. 66 (3), 2033–2043.
Li, S.E., Guo, Q., Xu, S., Duan, J., Li, S., Li, C., Su, K., 2017b. Fuel-saving predictive control for adaptive cruise control system considering road elevation information. IEEE Trans. Intell. Vehicl. (99), 1–12.
Li, S.E., Li, R., Wang, J., Hu, X., Cheng, B., Li, K., 2017c. Stabilizing periodic control of automated vehicle platoon with minimized fuel consumption. IEEE Trans. Transport. Electrificat. 3 (1), 259–271.
Lin, Q., Zhang, Y., Verwer, S., Wang, J., 2018. MOHA: a multi-mode hybrid automaton model for learning car-following behaviors. IEEE Trans. Intell. Transport. Syst. https://doi.org/10.1109/TITS.2018.2823418.
Lioris, J., Pedarsani, R., Tascikaraoglu, F.Y., Varaiya, P., 2017. Platoons of connected vehicles can double throughput in urban roads. Transp. Res. Part C 77, 292–305.
Milanes, V., Alonso, J., Bouraoui, L., Ploeg, J., 2011. Cooperative maneuvering in close environments among cybercars and dual-mode cars. IEEE Trans. Intell. Transport. Syst. 12 (1), 15–24.
Milanes, V., Shladover, S.E., 2014. Modeling cooperative and autonomous adaptive cruise control dynamic responses using experimental data. Transp. Res. Part C 48, 285–300.
Monteil, J., Bouroche, M., 2016. Robust parameter estimation of car-following models considering practical non-identifiability. In: 2016 IEEE 19th International Conference on Intelligent Transportation Systems (ITSC). pp. 581–588.
Moser, D., Schmied, R., Waschl, H., del Re, L., 2018. Flexible spacing adaptive cruise control using stochastic model predictive control. IEEE Trans. Control Syst. Technol. 26 (1), 114–127.
Orlov, Y., Belkoura, L., Richard, J.-P., Dambrine, M., 2003. Adaptive identification of linear time-delay systems. Int. J. Robust Nonlinear Control 13, 857–872.
Orosz, G., 2016. Connected cruise control: modeling, delay effects, and nonlinear behavior. Vehicle Syst. Dyn. 54 (8), 1147–1176.
Orosz, G., Ge, J.I., He, C.R., Avedisov, S.S., Qin, W.B., Zhang, L., 2017. Seeing beyond the line of sight - controlling connected automated vehicles. ASME Mech. Eng. Mag. 139 (12), S8–S12.
Orosz, G., Wilson, R.E., Stépán, G., 2010. Traffic jams: dynamics and control. Philosoph. Trans. Roy. Soc. A 368 (1928), 4455–4479.
Ploeg, J., Shukla, D., van de Wouw, N., Nijmeijer, H., 2014a. Controller synthesis for string stability of vehicle platoons. IEEE Trans. Intell. Transport. Syst. 15 (2), 845–865.
Ploeg, J., van de Wouw, N., Nijmeijer, H., 2014b. $\mathscr{L}_p$ string stability of cascaded systems: application to vehicle platooning. IEEE Trans. Control Syst. Technol. 22 (2), 786–793.
Qin, W.B., Orosz, G., 2017. Scalable stability analysis on large connected vehicle systems subject to stochastic communication delays. Transp. Res. Part C 83, 39–60.
Sadeghpour, M., Orosz, G., 2018. Can a finite number of discrete delays approximate stochastic delay? Syst. Control Lett. 116, 27–31.
Seiler, P., Pant, A., Hedrick, K., 2004. Disturbance propagation in vehicle strings. IEEE Trans. Automatic Control 49 (10), 1835–1842.
Shladover, S., Su, D., Lu, X.-Y., 2012. Impacts of cooperative adaptive cruise control on freeway traffic flow. Transport. Res. Rec.: J. Transport. Res. Board 2324, 63–70.
Shladover, S.E., Nowakowski, C., Lu, X.-Y., Ferlis, R., 2015. Cooperative adaptive cruise control definitions and operating concepts. Transport. Res. Rec.: J. Transport. Res. Board 2489, 145–152.
Treiber, M., Kesting, A., Helbing, D., 2006. Delays, inaccuracies and anticipation in microscopic traffic models. Physica A 360 (1), 71–88.
van Arem, B., van Driel, C.J.G., Visser, R., 2006. The impact of cooperative adaptive cruise control on traffic-flow characteristics. IEEE Trans. Intell. Transport. Syst. 7 (4), 429–436.
van Nunen, E., Kwakkernaat, R.J.A.E., Ploeg, J., Netten, B.D., 2012. Cooperative competition for future mobility. IEEE Trans. Intell. Transport. Syst. 13 (3), 1018–1025.
Vander Werf, J., Shladover, S., Miller, M., Kourjanskaia, N., 2002. Effects of adaptive cruise control systems on highway traffic flow capacity. Transport. Res. Rec.: J. Transport. Res. Board 1800, 78–84.
Wang, M., 2018. Infrastructure assisted adaptive driving to stabilise heterogeneous vehicle strings. Transp. Res. Part C 91, 276–295.
Wang, M., Daamen, W., Hoogendoorn, S.P., van Arem, B., 2014. Rolling horizon control framework for driver assistance systems. Part II: Cooperative sensing and cooperative control. Transport. Res. Part C 40, 290–311.
Zhang, L., Orosz, G., 2016. Motif-based analysis of connected vehicle systems: delay effects and stability. IEEE Trans. Intell. Transport. Syst. 17 (6), 1638–1651.
Zhang, L., Sun, J., Orosz, G., 2018. Hierarchical design of connected cruise control in the presence of information delays and uncertain vehicle dynamics. IEEE Trans. Control Syst. Technol. 26 (1), 139–150.
Zhao, W., Ngoduy, D., Shepherd, S., Liu, R., Papageorgiou, M., 2018. A platoon based cooperative eco-driving model for mixed automated and human-driven vehicles at a signalised intersection. Transport. Res. Part C.
Zhou, Y., Ahn, S., Chitturi, M., Noyce, D.A., 2017. Rolling horizon stochastic optimal control strategy for acc and cacc under uncertainty. Transp. Res. Part C 83, 61–76.